Biomaterials Science

ROYAL SOCIETY OF CHEMISTRY

PAPER

View Article Online
View Journal | View Issue

Cite this: *Biomater. Sci.*, 2025, **13**, 1233

Bioorthogonal reaction-mediated photosensitizer–peptide conjugate anchoring on cell membranes for enhanced photodynamic therapy†

Buwei Hu,[a,c] Chenlin Ji,[c,d] Zhuohang Zhou,[c] Xuehan Xu,[c,d] Luyi Wang,[c,d] Tingting Cao,[c,d] Jianjun Cheng *[b,c,e] and Rui Sun *[c,e]

Photodynamic therapy (PDT), utilizing a photosensitizer (PS) to induce tumor cell death, is an effective modality for cancer treatment. PS–peptide conjugates have recently demonstrated remarkable antitumor potential in preclinical trials. However, the limited cell membrane binding affinity and rapid systemic clearance have hindered their transition to clinical applications. To address these challenges, we investigated whether *in vivo* covalent chemistry could enhance tumor accumulation and potentiate antitumor efficacy. Specifically, we synthesized a PS–peptide conjugate termed P-DBCO-Ce6, with chlorin e6 (Ce6) and dibenzocyclooctyne (DBCO) conjugated to a negatively charged short peptide. By employing metabolic glycoengineering and bioorthogonal reactions, P-DBCO-Ce6 achieves covalent bonding to the cell membrane, enabling prolonged retention of the PS on the cell surface and the *in situ* generation of reactive oxygen species (ROS) on cell membranes to kill tumor cells. *In vivo* studies demonstrated a 3.3-fold increase in tumor accumulation of the PS through bioorthogonal reactions compared to the control group, confirming that click chemistry can effectively enhance PS tumor accumulation. This approach allows for the effective elimination of tumors with a single treatment. The improved efficiency of this strategy provides new insights into the design of PDT systems for potential clinical applications.

Received 30th November 2024,
Accepted 6th January 2025

DOI: 10.1039/d4bm01602e

rsc.li/biomaterials-science

Introduction

Photodynamic therapy (PDT) has emerged as an effective treatment modality for cancer and actinic keratosis, offering the advantages of minimal invasiveness and high therapeutic selectivity.[1–3] During PDT for tumors, the photosensitizer (PS) is a critical component, as it generates reactive oxygen species (ROS) within the tumor microenvironment upon laser excitation, thereby inducing cancer cell death.[4,5] However, the lack of *in vivo* specificity and limited tumor accumulation of PSs lead to insufficient solid tumor eradication efficiency in clinical PDT treatments.[6,7] Clinical PDT often requires the administration of excessive amounts of PSs and multiple treatment sessions, which can result in skin stimulation syndrome and potential eye damage.[8–10]

To overcome these challenges, a variety of PS delivery systems have been developed. Notably, short peptides, a class of biomaterials with diverse biofunctions, have emerged as potential solutions to enhance PS solubility and improve its *in vivo* delivery specificity.[11–13] The hydrophobic amino acids within peptides can interact with PSs through π–π interactions and co-assemble to form nanoparticles, thereby improving the PS loading efficiency and treatment outcome.[14–17] However, the aggregation of PSs in nanoparticles can diminish the ROS generation efficiency due to quenching of laser excitation.[18] On the other hand, peptides can be engineered to target cellular organelles or markers *via* their sequential structures.[13,19–21] A range of PS–peptide conjugates with subcellular organelle targeting properties has been developed, enabling the targeting of the endoplasmic reticulum, mitochondria, cell nucleus, and membrane.[22–25] Cell membranes targeting PSs can generate ROS and disrupt membrane stability, thereby inducing cell apoptosis or necrosis.[26–28] However, PS–peptide conjugates exhibit low ligand binding affinity and are still rapidly cleared

[a]*Department of Materials Science, Fudan University, Shanghai 200433, China*
[b]*Research Center for Industries of the Future, Westlake University, Hangzhou, Zhejiang 310030, China*
[c]*School of Engineering, Westlake University, Hangzhou, Zhejiang 310023, China*
[d]*School of Materials Science and Engineering, Zhejiang University, Hangzhou, Zhejiang 310023, China*
[e]*Institute of Advanced Technology, Westlake Institute for Advanced Study, Hangzhou, Zhejiang 310023, China. E-mail: chengjianjun@westlake.edu.cn, sunrui14@westlake.edu.cn*

† Electronic supplementary information (ESI) available. See DOI: https://doi.org/10.1039/d4bm01602e

in vivo, showing that multiple treatment sessions are still inevitable for effective tumor treatment.[29,30]

Previous *in vivo* studies combining metabolic glycoengineering with bioorthogonal reactions have demonstrated a promising performance in tumor targeting drug delivery through a two-step strategy.[31–33] Unnatural sugars, including tetraacetyl-*N*-azidoacetylmannosamine (Ac_4ManNAz, AAM) and its derivatives, have been developed to introduce artificial azide labels on the cell surface by utilizing the sialic acid synthesis pathway.[34–38] Due to metabolic preferences, cancer cells tend to produce more sialic acid during glycosylation, and consequently, can present more artificial ligands on their surface compared to normal cells.[39–41] Leveraging this characteristic, *in vivo* click chemistry has shown advantages in tumor imaging, drug targeting delivery, and enhanced tumor penetration.[42–44] Furthermore, the click reaction can form covalent bonding between cells and the dibenzocyclooctyne (DBCO)-decorated cargo. The irreversible bond between cells and ligands can facilitate drug accumulation in tumors and achieve better treatment outcomes.[45–47]

Inspired by recent advancements, we synthesized a PS–peptide conjugate adorned with DBCO groups, denoted as P-DBCO-Ce6. The amphiphilic nature of P-DBCO-Ce6 enhances its capability for tumor accumulation. By employing metabolic glycoengineering and bioorthogonal chemistry, P-DBCO-Ce6 is conjugated to the cell membrane, thereby extending the residence time of PSs on the cell surface and directly killing tumor cells by *in situ* ROS generation. Our *in vivo* studies have revealed a significant 3.3-fold increase in PS tumor accumulation with the assistance of click chemistry compared to the control. This innovative approach holds the potential for effective tumor ablation within a single treatment session.

Experimental

Materials and devices

Fmoc-Lys(Boc)-OH and Fmoc-Glu(OtBu)-OH were obtained from GL Biochem Ltd (Shanghai, China). 11,12-Didehydro-γ-oxo-dibenzazocine-5(6*H*)-butanoic acid 2,5-dioxo-1-pyrrolidinyl ester (DBCO-NHS Ester) was obtained from Jiangsu Aikang Biopharmaceutical Co., Ltd (Nanjing, China). Tetraacetyl-*N*-azidoacetylmannosamine (AAM) was obtained from Aladdin Co., Ltd (Shanghai, China). Chlorin e6 (Ce6) was obtained from J&K Scientific Co., Ltd. All mentioned biological assay kits were obtained from Beyotime Biotechnology Co., Ltd (Shanghai, China). Hoechst 33342, DAPI, and CellMask Orange were obtained from Thermo Fisher Scientific Co., Ltd (USA). C11-BODIPY, DBCO-Cy5, DBCO-biotin, and streptavidin–horseradish peroxidase (HRP) were obtained from Sigma-Aldrich Co., Ltd (USA). All other chemical reagents were obtained from Sinopharm Chemical Reagent Co., Ltd (Shanghai, China). All antibodies were obtained from Abcam Co., Ltd (Shanghai, China). All reagents were used as received without further purification or treatment.

Nuclear magnetic resonance (NMR) spectra were acquired on a Bruker Avance III 600 spectrometer using deuterated solvents. The UV-Vis spectrum absorbance was collected with a Shimadzu UV-2600i (Kyoto, Japan). Peptides were synthesized using a Liberty Blue HT24 multi-channel microwave-assisted peptide synthesizer from CEM (Matthews, USA). Cellular toxicities were assessed using a Spectramax Max i5 microplate reader. Cellular fluorescence detection was analyzed using CytoFLEX (Becton Dickinson Caliper) and a confocal laser scanning microscope (CLSM, Carl Zeiss 980). Images of tumor-bearing mice were captured using a small animal imaging system (IVIS, PE Spectrum, Waltham, USA). Protein bands were visualized using a Bio-Rad ChemiDoc MP imaging system (Hercules, USA). All laser radiation experiments were conducted using an HC0004-4 660 nm laser source from UltraDurability Technology (Jian, China). The size and ζ-potential of nanoparticles were analysed by using a Bruker dynamic light scattering refractometer (Massachusetts, USA).

Synthesis of P-Ce6 and P-DBCO-Ce6

The peptide was prepared on 2-chlorotrityl chloride resin (0.135 g, 0.74 mmol g^{-1}, 1 equiv.). The first amino acid, Fmoc-Glu(OtBu)-OH (34.1 mg, 0.8 equiv.), and DIPEA (78.6 μl, 4.5 equiv.) in a 2 ml DCM solution were added to the resin, and the mixture was shaken for 1.5 h at room temperature (RT) to conjugate the first amino acid to the resin. The resin was then washed sequentially with DCM (3 × 5 mL), DMF (3 × 5 mL), and i-PrOH (3 × 5 mL), and dried overnight under vacuum. The remaining active sites on the resin were capped using a mixture of DCM/MeOH/DIPEA (85 : 10 : 5, v/v/v) for 15 min at RT, followed by washing with DMF (3 × 5 mL) and DCM (3 × 5 mL). The resin was then subjected to iterative peptide assembly (Fmoc-SPPS). The K_4E_4-resin short peptide was synthesized using a CEM multi-channel microwave-assisted peptide synthesizer, following the manufacturer's instructions.

To synthesize P-Ce6, Ce6 (20 mg, 0.03 mmol, 1 equiv.) was functionalized with EDC·HCl (7.07 mg, 0.033 mmol, 1.1 equiv.) and NHS (4.63 mg, 0.036 mmol, 1.2 equiv.) in DMF at RT for 2 h. This mixture was then added to the K_4E_4-resin (50 mg) and shaken for 48 h at RT. The resin was washed with DCM (3 × 5 mL) to remove free Ce6. Then, P-Ce6 was cleaved using a solution of DCM/trifluoroacetic acid (TFA)/triisopropylsilane (89/10/1, v/v/v) for 3 h at RT. The product, P-Ce6, was extracted with water and characterized by matrix-assisted laser desorption/ionization time-of-flight mass spectrometry (MALDI-TOF-MS) and ^{1}H nuclear magnetic resonance (^{1}H NMR).

For the preparation of P-DBCO-Ce6, P-Ce6 (10 mg, 0.006 mmol, 1 equiv.) and DBCO-NHS (12.3 mg, 0.03 mmol, 5 equiv.) were dissolved in a 10% triethylamine (TEA)/DMF solution and stirred at RT overnight. The product was dialyzed against DMF (6 × 0.5 L) for 2 days, followed by dialysis in water (6 × 2 L) for another 2 days, and then lyophilized. The final product was characterized by MALDI-TOF-MS and ^{1}H NMR.

Optical and ROS generation functionality assay

The absorption spectra of Ce6, P-Ce6, and P-DBCO-Ce6 (5 μM) in PBS or methanol were recorded by using a UV-Vis spectrophotometer. The ROS generation efficiency of P-DBCO-Ce6 was

assessed by using the 9,10-anthracenediyl-bis(methylene)dimalonic acid (ABDA) method. A mixture of Ce6 or P-DBCO-Ce6 (50 μM) with ABDA (100 μM) in 1.5 mL of PBS was exposed to a 660 nm laser at an intensity of 30 mW cm^{-2} for 5 min. Samples were taken every 30 s and the absorption of ABDA was detected at 378 nm using a plate reader. The detection of singlet oxygen ($^1O_2$), hydroxyl radicals ($^{\bullet}OH$), and superoxide anion ($O_2^{\bullet-}$) generation was conducted following the protocol described previously.[28]

Cell culture

Human glioblastoma cells (U251), human breast cancer cells (MDA-MB-231), and human bladder cancer cells (T24) were obtained from ATCC (Manassas, USA) and incubated in a normal cell culture medium consisting of DMEM supplemented with 10% heat-inactivated FBS (fetal bovine serum), penicillin (100 units per mL), and streptomycin (100 μg mL^{-1}). The cells were cultured in an incubator under a 5% CO_2 atmosphere at 37 °C. All cell culture consumables were obtained from Wisent Inc., Ltd (Canada).

In vitro metabolic glycoengineering and characterization

For azide labeling, cells were cultured in normal cell culture medium supplemented with AAM (50 μM) and incubated for three days. Azide labeled cells were analyzed by western blotting following a previously reported procedure.[21] Briefly, azido-modified biomacromolecules in cell lysates were biotinylated by incubation with DBCO-biotin. Then, streptavidin-HRP and an enhanced chemiluminescence (ECL) kit were used to detect the HRP signal on the membrane with a ChemiDoc Imaging System.

Azide-labeled cells were further analyzed by flow cytometry. Cells with or without AAM treatment were seeded into 12-well plates at a density of 1×10^5 cells per well. Afterward, cells were washed with PBS three times, and a DBCO-Cy5 (50 μM) solution was incubated with the cells for 1 h at 37 °C. Fluorescence signals on the cells were detected by flow cytometry.

In vitro cell surface click reaction analysis

To investigate the cell surface click reaction kinetics, T24 cells treated with or without AAM were seeded into 12-well plates at a density of 1×10^5 cells per well and cultured overnight. Then, cells were washed with PBS three times and incubated with P-DBCO-Ce6 solutions at different concentrations (1.56, 3.12, 6.25, 12.5, and 25 μM) for 30 min. Finally, the cells were washed with PBS three times and collected for flow cytometry analysis.

To investigate the time-dependent click reaction kinetics, similar instructions used in the concentration study were followed. Cells were incubated with P-DBCO-Ce6 (25 μM) at 37 °C for different durations (1, 3, 5, 15, and 30 min). After incubation, the cells were collected and analyzed by using flow cytometry.

P-DBCO-Ce6 cell membrane targeting and retention analysis

T24 cells with or without AAM pre-treatment were seeded into confocal dishes at a density of 1×10^4 cells per dish. After overnight incubation, the cells were treated with P-DBCO-Ce6 (50 μM) after being washed with PBS three times, and incubated for 1 h at 37 °C. Then, the cells were stained with CellMask Orange (1 μg mL^{-1}) for 15 min at RT for cell membrane labeling, and with Hoechst (2 μg mL^{-1}) for 10 min at 37 °C. All observations were completed by using the CLSM system.

To analyze the cell surface retention status of P-DBCO-Ce6, the same cell treatment procedure was followed as described above. Cells were observed at different time points (0, 6, 12 and 24 h) after treatment with P-DBCO-Ce6 for 1 h at 37 °C by using the CLSM system.

In vitro cell cytotoxicity of Ce6, P-Ce6 and P-DBCO-Ce6

Cells were treated with or without AAM and seeded into 96-well plates at a density of 5000 cells per well and cultured overnight to allow attachment. Then, the culture media were removed, and fresh media containing various concentrations of Ce6, P-Ce6, or P-DBCO-Ce6 (0–5 μM) were added. Cells were co-cultured with these agents for 5 min, followed by three washes with PBS. For photo cytotoxicity, cells were irradiated with a 10 mW cm^{-2} 660 nm laser source for 5 min and then incubated overnight. For dark cytotoxicity, cells were incubated overnight without irradiation. Cell viability was analyzed using the methyl thiazolyl tetrazolium (MTT) assay, following the kit instructions.

Cell death analysis

Cell apoptosis assay. Annexin-V/PI (Beyotime) was employed to assess cell apoptosis following the standard protocols. T24 cells were treated with or without AAM and seeded into 12-well plates at a density of 1×10^5 cells per well and cultured overnight. P-DBCO-Ce6 (1 μM) was added to the cells and incubated for 5 min, followed by three washes with PBS. Cells were then irradiated with a 10 mW cm^{-2} 660 nm laser source for 5 min. The cells were processed according to the Annexin-V/PI assay kit instructions and analyzed for cell death stages by flow cytometry.

Live and dead staining analysis. T24 cells were seeded into confocal dishes at a density of 1×10^4 cells and cultured overnight. After treating the cells under the same conditions as the apoptosis assay, we used the Live & Dead staining kit (Beyotime) to evaluate the cell death status.

In vitro ROS generation analysis

In vitro ROS generation was assessed by CLSM and flow cytometry. Briefly, T24 cells treated with or without AAM were incubated with 1 μM P-DBCO-Ce6 for 5 min, followed by three washes with PBS. A ROS detection probe (Beyotime) was applied to the cells according to the manufacturer's instructions. Cells were then irradiated with a 660 nm laser at 10 mW cm^{-2} for 5 min. CLSM was employed to visualize the fluo-

rescence signal, and flow cytometry was used to quantify the signal intensity.

Cell membrane damage analysis

C11-BODIPY staining analysis. T24 cells were seeded into confocal dishes at a density of 1×10^4 cells and cultured overnight. Cells were then incubated with C11-BODIPY (10 μM) for 30 min. Subsequently, cells were treated with Ce6, P-Ce6, or P-DBCO-Ce6 (25 μM) for 10 min. Finally, cells were irradiated with a 660 nm laser at 40 mW cm^{-2} for 10 min, and CLSM was used to analyze the fluorescence changes.

Intracellular malondialdehyde (MDA) assay. Similar to the C11-BODIPY CLSM analysis, T24 cells were seeded into 6-well plates at a density of 1×10^6 cells and cultured overnight. Cells were then treated with the same PSs and laser conditions as in the C11-BODIPY experiment. Post-treatment, cell lysis buffer was used to obtain the cell lysate. The MDA assay protocol (Beyotime) was followed to determine the MDA concentration in the cell lysate. The BCA assay kit was used to measure the protein concentration, and the relative MDA generation levels were normalized to the protein concentration.

Mouse maintenance

Mouse experiments were conducted with the approval of the Animal Care and Use Committee of Westlake University. The mice were sourced from GemPharmatech Co., Ltd (Jiangsu, China) and raised under standard conditions. All animal procedures were performed in accordance with the Guidelines for Care and Use of Laboratory Animals of Westlake University and approved by the Animal Ethics Committee of Laboratory Animal Resource Center, Westlake University. Female BALB/c nude mice (17–22 g) were used to establish the tumor-bearing mouse models. The suspension of T24 cells (5×10^7 cells per mL, 0.1 mL) was injected into the right hind flank of each mice. Tumor volume (V) was calculated using the formula: $V = (L \times W^2)/2$ (mm^3), where L represents the length and W represents the width of the tumor, respectively.

In vivo biodistribution study

AAM was encapsulated within liposomes following the protocol described previously.[48] The size and ζ-potential of AAM liposomes were analysed by dynamic light scattering (DLS) and particle electrophoretic mobility. Mice were administered Ce6, P-Ce6, or P-DBCO-Ce6 at a dosage of 2 μM kg^{-1} Ce6. For the AAM+P-DBCO-Ce6 group, AAM was administered intravenously at a dosage of 100 mg kg^{-1} for 3 days prior to the administration of P-DBCO-Ce6. Mice (n = 4) were analyzed using the IVIS under the 660/765 channel at various time points following administration treatment. After a 48 h observation period, mice were sacrificed, and tumors along with organs (heart, liver, spleen, lungs, and kidneys) were extracted and further analyzed by using the IVIS system.

In vivo PDT anti-tumor efficiency study and blood chemistry analysis

Tumor-bearing mice were randomly divided into 5 groups (n = 6 for each group): PBS, Ce6, P-Ce6, P-DBCO-Ce6, and AAM+P-DBCO-Ce6. Following the administration protocol described in the biodistribution study, a 660 nm laser radiation treatment was conducted 6 h after various PS administration. Each mouse was subjected to irradiation with a 120 mW cm^{-2} laser for 15 min. Tumor size and body weight were monitored and recorded at regular intervals throughout the experiment. After the experiment, all mice were sacrificed, and tumors were excised, weighed, and fixed in formalin. Blood was collected from each mouse prior to sacrifice and subjected to standard biochemical analysis.

AAM biosafety analysis

The tumor-bearing mice were randomly divided into 2 groups (n = 6 per group). Following the AAM administration protocol described in the biodistribution study, tumor size and body weight were monitored and recorded throughout the experiment. After the experiment, all mice were sacrificed, and the tumors were excised, weighed, and fixed in formalin.

Histological examination of tissues

The fixed tumors and organs were embedded in paraffin and sectioned into 5 μm thick slices. These slices were then stained with hematoxylin and eosin (H&E) for histological examination and subsequently observed under an inverted microscope.

Statistical analysis

Statistical analyses were conducted using GraphPad Prism version 10.3.0. To compare the two groups, we utilized an unpaired, two-tailed Student's t-test with a 95% confidence interval. $^*p < 0.05$, $^{**}p < 0.01$, $^{***}p < 0.001$, and $^{****}p < 0.0001$ were considered statistically significant.

Results and discussion

The synthesis and characterization of P-DBCO-Ce6

Ce6, an FDA-approved PS, is extensively used in cancer PDT. Despite its efficacy, its high hydrophobicity significantly limits its solubility in water, posing a challenge for therapeutic applications.[49] To overcome this issue, Ce6 has been conjugated with peptides to enhance its solubility. Although this modification has successfully improved solubility, it has been observed that the peptide conjugated Ce6 exhibits inadequate tumor accumulation.[50] In this study, we rationally designed a Ce6–peptide conjugate adorned with DBCO to evaluate its potential to enhance tumor retention through bioorthogonal reaction-mediated mechanisms and to potentiate antitumor efficacy (Fig. 1a). The synthetic procedures are detailed in Fig. S1.† Briefly, we synthesized a Ce6–peptide conjugate Ce6-K_4E_4 (named P-Ce6) using SPPS. Subsequently, DBCO-NHS was conjugated to obtain the final product, P-DBCO-Ce6, with a

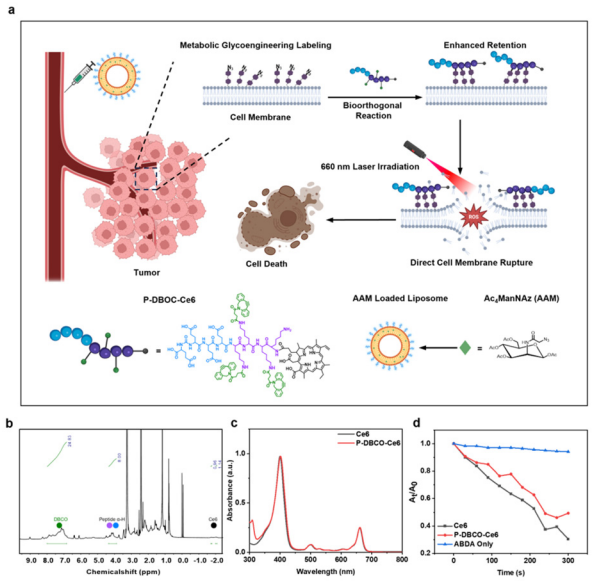

Fig. 1 Schematic representation of the working mechanism, structure and properties of P-DBCO-Ce6. (a) Schematic illustration of the working mechanism of P-DBCO-Ce6; (b) ^{1}H NMR characterization of P-DBCO-Ce6 in *d6*-DMSO; (c) UV-Vis absorption spectrum of P-DBCO-Ce6 and Ce6 in methanol; and (d) total reactive oxygen species (ROS) generation by P-DBCO-Ce6 and Ce6, as detected by ABDA (100 μM) under 660 nm laser irradiation (30 mW cm^{-2}) for various time intervals.

48% yield. Characterization of the synthesized compounds was performed using ^{1}H NMR, and MALDI-TOF-MS, confirming the successful synthesis of P-Ce6 (Fig. S2 and S3†) and P-DBCO-Ce6 (Fig. 1b and Fig. S4†). To evaluate the optical properties of Ce6 after decoration, the absorbance spectra of P-Ce6 (Fig. S5†) and P-DBCO-Ce6 (Fig. 1c) were analyzed. The results revealed that, after conjugation, P-Ce6 and P-DBCO-Ce6 UV-Vis absorbance profiles were similar to that of Ce6, indicating that the optical properties of Ce6 were preserved. Under physiological conditions, P-DBCO-Ce6 displayed a slight red shift in its absorbance peak at around 660 nm, which we attribute to the self-assembly of the short peptide (Fig. S6†).[13] The critical micelle concentration (CMC) measurement was further conducted to demonstrate the self-assembling properties of P-DBCO-Ce6. The results showed that P-DBCO-Ce6 has a CMC value of 0.83 μM (Fig. S7†). The CMC experiment indicated that P-DBCO-Ce6 is capable of forming self-assembled structures under physiological conditions. The ROS generated by Ce6 is the key functional molecule in the PDT treatment. Therefore, the ROS generation capability of P-DBCO-Ce6 was investigated by using ABDA as a singlet oxygen indicator.[51] The decrease in ABDA absorbance upon exposure to a 660 nm laser confirmed the generation of ROS. P-DBCO-Ce6 demonstrated a slightly lower singlet oxygen production rate compared to free Ce6, potentially due to the alkyl group in DBCO consuming the ROS generated under light irradiation (Fig. 1d).[52] The influence of DBCO on the type of ROS generated was further analyzed using probes responsive to specific ROS types.[53,54] The results further demonstrated that chemical modifications have a minimal impact on the functionality of Ce6 (Fig. S8†), thereby allowing for subsequent research in PDT.

Cell surface bioorthogonal reaction and cell membrane targeting analysis

The quantity of sialic acid on the cell surface, a determinant of azide group incorporation through metabolic glycoengineering, consequently influences the rate and efficiency of bioorthogonal reactions at the cell surface. Initially, we evaluated the labeling efficiency of sialic acid azide in three commonly utilized cell lines: U251, MDA-MB-231, and T24, employing western blot analysis as previously established methods[36] (Fig. 2a and Fig. S9 and S10†). Our findings revealed that T24 cells exhibited the highest expression of sialic acid with azide labeling, surpassing those of U251 and

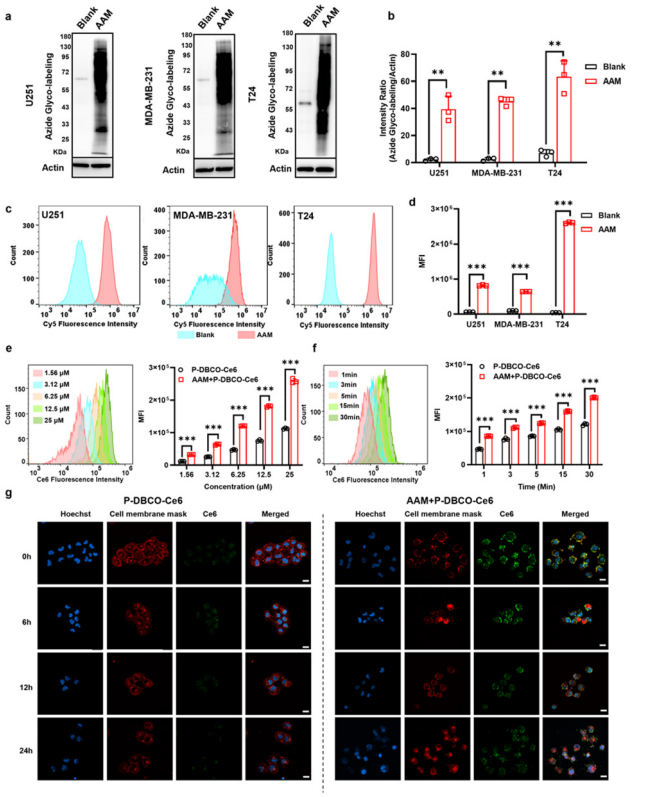

Fig. 2 Cell surface azide labeling and click reaction analysis. (a) Western blot analysis of azide glycol labeling in U251, MDA-MB-231, and T24 cells; (b) statistical analysis of the western blot results; (c) flow cytometry analysis of the DBCO-Cy5 click reaction with U251, MDA-MB-231, and T24 cells; (d) statistical analysis of the flow cytometry results; and (e) concentration-dependent kinetics of the cell surface click reaction with P-DBCO-Ce6, with or without AAM labeling. P-DBCO-Ce6 was incubated with cells for 30 min; (f) time-dependent kinetics of the cell surface click reaction with P-DBCO-Ce6 (25 μM), with or without AAM labeling; and (g) CLSM images of P-DBCO-Ce6 cell surface retention with or without azide labeling at different time points after the treatment. Cells were incubated with 50 μM P-DBCO-Ce6 for 1 h at 37 °C. Scale bar: 20 μm (*$p < 0.05$, **$p < 0.01$ and ***$p < 0.001$).

MDA-MB-231 cells (Fig. 2b). Further validation was provided by flow cytometry analysis, which corroborated the higher sialic acid expression on the cell surface of T24 cells (Fig. 2c and d). Based on these compelling results, T24 cells were selected as the model system for our subsequent experimental investigations.

We investigated the kinetics of the cell surface bioorthogonal reaction to illustrate the binding progress of P-DBCO-Ce6. T24 cells were incubated with AAM for 3 days before examining the cell surface conjugation of P-DBCO-Ce6. Flow cytometry analysis revealed that the conjugation of P-DBCO-Ce6 to the cell surface was both time- and concentration-dependent (Fig. 2e and f). Statistical analysis of the mean fluorescence intensity (MFI) indicated that the cell surface click reaction could occur within 1 min, resulting in a significant enhancement in P-DBCO-Ce6 attachment. Furthermore, the bioorthogonal reaction increased the cell attachment efficiency of P-DBCO-Ce6 by approximately 40% compared to the interaction between T24 cells and P-DBCO-Ce6. We also assessed the cell absorption efficiency of P-Ce6 on the cell surface, which was also time- and concentration-dependent (Fig. S11†), but it was two orders of magnitude lower than that of P-DBCO-Ce6 on the untreated cells (Fig. S12†). Subsequently, to further investigate the subcellular distribution of the bioorthorgonal reaction, the cell surface conjugation of P-DBCO-Ce6 was examined using confocal laser scanning microscope (CLSM) imaging. Notably, P-DBCO-Ce6 exhibited significantly higher cell membrane attachment efficiency and was found to be highly colocalized with the cell membranes, as compared to the cells that did not receive AAM treatment (Fig. S13†).

In clinical practice, PDT is typically initiated several hours or days following the administration of the PS. Therefore, we further analyzed the bioorthogonal reaction-mediated cell surface retention time of the PS. After treating T24 cells with P-DBCO-Ce6 for 1 h, CLSM imaging was employed to assess the localization of P-DBCO-Ce6 at various time intervals post-treatment (Fig. 2g). Notably, P-DBCO-Ce6 conjugated on the cell surface demonstrated remarkable retention on the cell membrane for up to 24 h. In contrast, cells without AAM treatment showed a tendency to endocytose P-DBCO-Ce6. The surface click reaction mediated the sustained retention of P-DBCO-Ce6 on the cell surface, providing an ample therapeutic window for PDT in both clinical and *in vivo* applications. Furthermore, the reduction of PS endocytosis prevented rapid degradation of the peptide–PS conjugate in the lysosome, preserving more PS on the cell membrane for efficient PDT treatment. This characteristic ensures prolonged targeting of the cell membrane, enabling multiple laser treatments within a single PS dose, and thus further extending the clinical application potential of P-DBCO-Ce6.

In vitro cell cytotoxicity and cell death mechanism study

Light-induced cytotoxicity is a pivotal determinant of PS efficacy in PDT.[55] We hypothesized that the bioorthogonal reaction-mediated cell surface retention of P-DBCO-Ce6 could directly disrupt cancer cell membranes *via* the *in situ* generation of ROS. Initially, we performed MTT assays to compare the dark toxicity and phototoxicity of P-DBCO-Ce6 on T24 cells with and without AAM treatment (Fig. 3a). Cells were incubated with P-DBCO-Ce6 for 5 min, followed by phosphate-buffered saline (PBS) washing to remove unbound PS. For photocytotoxicity assessment, cells were irradiated with a 660 nm laser at an intensity of 10 mW cm^{-2} for an additional 5 min. P-DBCO-Ce6 showed no significant dark toxicity but exhibited phototoxicity in T24 cells, particularly in those treated with AAM. This enhancement was ascribed to the bioorthogonal click reaction, which facilitated increased Ce6 retention on the cell surface. Additionally, we assessed the toxicity of free Ce6 and P-Ce6 under identical conditions, both in the presence and absence of light, and found no significant phototoxicity (Fig. S14†) or dark toxicity (Fig. S15†). This lack of toxicity was attributed to the minimal cell surface anchoring of these agents. To further validate the general applicability of our system, we extended our evaluation to MDA-MB-231 and U251 cells. Similar to T24 cells, Ce6 and P-Ce6 did not exhibit significant phototoxicity in these cell lines. In contrast, P-DBCO-Ce6 displayed pronounced cytotoxicity upon laser irradiation, suggesting that our system is robust against variations in sialic acid expression and has broad applicability (Fig. S16–S19†).

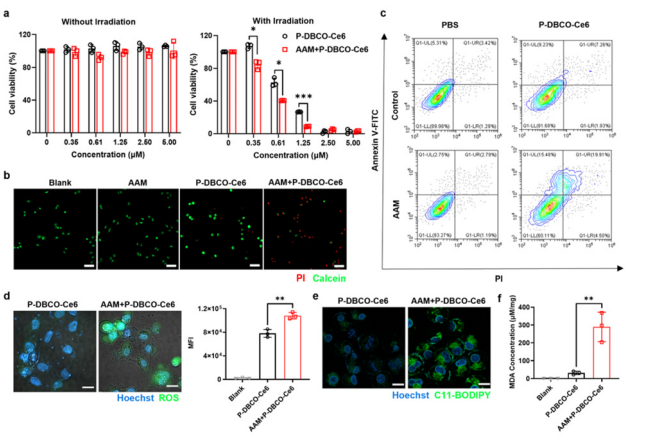

Fig. 3 *In vitro* cell toxicity assessment and investigation of the killing mechanism. (a) Phototoxicity and dark toxicity assessment of P-DBCO-Ce6 on T24 cells with or without AAM treatment (for phototoxicity, upon 660 nm laser irradiation, 10 mW cm^{-2}, 5 min); (b) live and dead staining of T24 cells pretreated with P-DBCO-Ce6 (1 μM, 5 min) after 660 nm laser excitation (10 mW cm^{-2}, 5 min), scale bar: 100 μm; (c) cell apoptosis analysis of T24 cells treated with P-DBCO-Ce6 (1 μM, 5 min) following 660 nm laser treatment (10 mW cm^{-2}, 5 min); (d) intracellular ROS generation detected by using a ROS fluorescent probe, imaged with CLSM and quantitatively analyzed with flow cytometry; T24 cells treated with P-DBCO-Ce6 (1 μM, 5 min) following 660 nm laser treatment (10 mW cm^{-2}, 5 min), scale bar: 20 μm; (e) CLSM imaging of C11-BODIPY excitation by ROS, generated from the cell surface attached PS (25 μM, 10 min) under laser irradiation (40 mW cm^{-2}, 10 min), scale bar: 20 μm; and (f) intracellular MDA levels in cells with different treatments after laser irradiation (*$p < 0.05$, **$p < 0.01$ and ***$p < 0.001$).

Given that membrane-anchored PSs can trigger necrosis and apoptosis, potentially initiating a systemic immune response and preventing tumor recurrence,[21,28,56] we further evaluated the cell death mechanism in our system. We initially employed Live & Dead staining to assess the cell membrane integrity. The findings revealed calcein release and propidium iodide (PI) nuclear translocation immediately post-PDT treatment (Fig. 3b), suggesting that P-DBCO-Ce6 induced cell death likely resulting from membrane rupture.[26,57] Subsequently, cell apoptosis assays were conducted to further dissect the cell death pathways following PDT. The cell surface click reaction significantly amplified the light-induced cytotoxicity of P-DBCO-Ce6, which underwent both necrosis and apoptosis (Fig. 3c).

With evidence indicating the possibility that cell membrane attached P-DBCO-Ce6 eliminates cancer cells through cell membrane rupture, we then investigated whether bioorthogonal reaction-mediated PDT enhances ROS generation at the cell membrane. Using a ROS detection kit and CLSM, we found that click reaction-mediated PDT induced higher ROS levels than non-reaction groups, correlating with cellular morphological changes indicative of membrane rupture (Fig. 3d and Fig. S20†). Under physiological conditions, ROS is a highly reactive molecule that can only diffuse to a limited area due to this property.[58,59] The *in situ* ROS production at the membrane may directly disrupt the cell membrane. Employing C11-BODIPY, a dye that inserts into the cell membrane and generates fluorescence upon oxidation by ROS, we observed the highest fluorescence intensity with click reaction-mediated PDT (Fig. 3e and Fig. S21a†), confirming membrane-targeted ROS damage. Given the complexity of the cell membrane and the essential role of lipids as a component, we hypothesized that click reaction-mediated PDT induced lipid oxidation, reducing cell membrane stability. Therefore, we assessed lipid damage using MDA as a biomarker.[60–62] Post-PDT treatment, click reaction-mediated PDT significantly increased MDA levels compared to other groups (Fig. 3f and Fig. S21b†), demonstrating that this approach achieves enhanced therapeutic efficacy through targeted cell membrane lipid damage.

In vivo photosensitizer biodistribution analysis

Bioorthogonal chemistry, characterized by its distinct reactive groups and minimal side reactions under physiological conditions, presents a promising strategy for tumor targeting.[63,64] We hypothesize that the amphiphilic nature of P-DBCO-Ce6 could enhance tumor enrichment, and the subsequent *in situ* bioorthogonal reaction could secure the prolonged retention of the PS within the tumor. To validate this hypothesis, we established T24 tumor-bearing mouse models and conducted *in vivo* biodistribution studies of P-DBCO-Ce6. When tumors reached a volume of approximately 120 mm^3, mice were intravenously administered with various PSs or AAM+PS, and their biodistribution was analyzed using IVIS at different time intervals after administration. The results revealed that Ce6 and P-Ce6 were rapidly cleared from the mice within 2 h and 6 h post-injection, respectively. In contrast, P-DBCO-Ce6 demonstrated an extended circulation time, likely due to its self-assembling properties, which facilitates accumulation at the tumor site *via* the enhanced permeability and retention (EPR) effect.[65] Furthermore, the ζ-potential measurement of P-DBCO-Ce6 revealed that it possesses a −15.7 mV negative charge, which prevents serum protein absorption and, consequently, prolongs blood circulation (Fig. S22†). Additionally, P-DBCO-Ce6 exhibits non-specific binding with cells *in vitro*, likely due to the hydrophobicity of the DBCO moiety. These non-specific interactions between P-DBCO-Ce6 and the cell membrane could potentially prolong the blood circulation time of P-DBCO-Ce6 and, in conjunction with the EPR effect, facilitate the targeting of photosensitizers to tumors. Moreover, the bioorthogonal reaction induced PS aggregation in tumors within the first 12 h and sustained retention for at least 48 h (Fig. 4a). Further analysis of organ distribution confirmed that bioorthogonal reaction-mediated PS accumulation in tumors enhanced delivery specificity and potentially mitigated the side effects associated with PDT (Fig. 4b). At 48 h post PS administration, quantification of accumulated PS in the tissues showed a 3.3-fold tumor enrichment of PSs in the AAM+P-DBCO-Ce6 group, compared to the mice in the P-DBCO-Ce6 group. Meanwhile, there was no significant change in P-DBCO-Ce6 accumulation in the main organs of mice (Fig. 4c). These findings suggest that *in vivo* bioorthogonal reactions significantly improve PS targeting and retention in tumors for at least 48 h, holding great potential for anti-tumor applications and further extending the therapeutic window of PDT.

In vivo antitumor assay and biosafety analysis

Given the above results demonstrating that the click reaction enhances both the phototoxicity and tumor retention of P-DBCO-Ce6, the antitumor efficacy of bioorthogonal reaction-

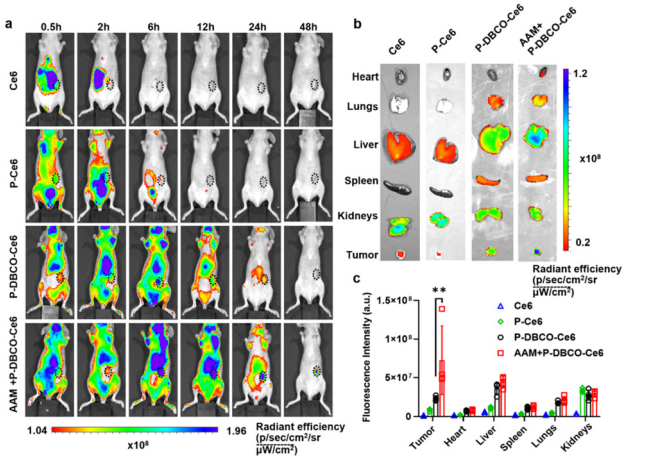

Fig. 4 *In vivo* biodistribution analysis. (a) *In vivo* biodistribution of Ce6, P-Ce6, P-DBCO-Ce6, and AAM+P-DBCO-Ce6 at different times. AAM was I.V. injected, 100 mg kg^{-1} for 3 consecutive days, once a day, and the PS was then administered with 2 μM kg^{-1} Ce6 concentration; (b) *ex vivo* imaging and (c) the corresponding fluorescence intensity of the tumor and major organs at 48 h post injection of Ce6, P-Ce6, P-DBCO-Ce6, and AAM+P-DBCO-Ce6 (*$p < 0.05$ and **$p < 0.01$).

mediated PDT needs further investigation. When tumors reached approximately 120 mm^3, mice were intravenously administered Ce6, P-Ce6, P-DBCO-Ce6, or AAM+P-DBCO-Ce6 at a Ce6 dosage of 2 μM kg^{-1}. Subsequently, a 660 nm laser with an intensity of 120 mW cm^{-2} was applied to the tumor site for 15 min, 6 h post various PS injection (Fig. 5a). Mice treated with PBS or AAM liposomes were used as controls. The size and charge of the AAM liposome did not show any dramatic changes based on DLS and ζ-potential analysis over a 10-day period. (Fig. S23†). Statistical analysis of tumor growth revealed that the PBS and AAM liposome groups followed similar tumor growth patterns without obvious tumor inhibition (Fig. S24 and S25†). The histological analysis also indicated that the AAM liposome did not show significant tissue damage (Fig S24c†). The AAM+P-DBCO-Ce6 group began to exhibit significant tumor reduction on day 2 after PDT. Although the P-DBCO-Ce6 group also demonstrated some antitumor effect, tumor regrowth was observed after day 10 (Fig. 5b). Tumor weight and histopathological data further illustrated that bioorthogonal reaction-mediated PDT could effectively eradicate tumors with minimum effect on the physiological conditions of the mice (Fig. 5d and e). After a single PDT session, the tumor size of the AAM+P-DBCO-Ce6 group was negligible (Fig. S26†). Subsequent analysis of *ex vivo* tumors revealed that in this group, the tumors in half of the mice were completely eradicated, illustrating impressive antitumor efficiency (Fig. 5c). H&E staining of tumor cryosections indicated that the AAM+P-DBCO-Ce6 group's tumor tissue had a looser density compared to the other groups (Fig. 5f).

Furthermore, we assessed the biosafety of the bioorthogonal reaction-mediated PDT. Post-treatment blood chemistry

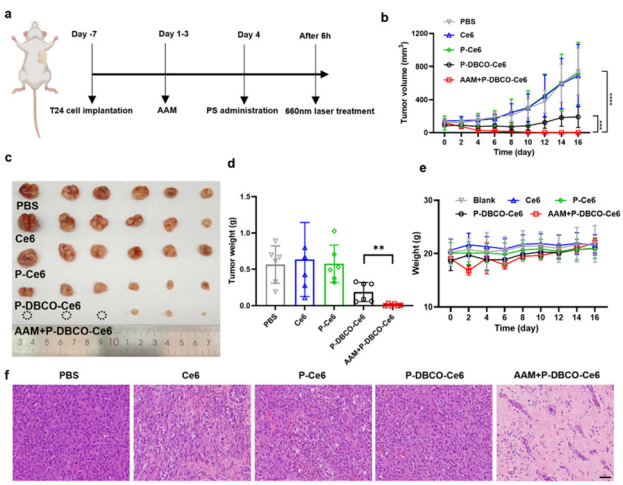

Fig. 5 Antitumor efficacy analysis. (a) Schematic representation of the *in vivo* tumor treatment regimen (660 nm laser irradiation, 120 mW cm^{-2}, 15 min); (b) tumor growth curves over a 16-day period in mice bearing T24 tumors; (c) illustration of tumors harvested on day 16; (d) weights of the harvested tumors on day 16; and (e) changes in the body weight of mice after PDT; (f) hematoxylin and eosin (H&E) staining of tumor tissues harvested from mice on day 16 post-PDT treatment, scale bar: 50 μm (*p < 0.05, **p < 0.01, ***p < 0.001 and ****p < 0.0001).

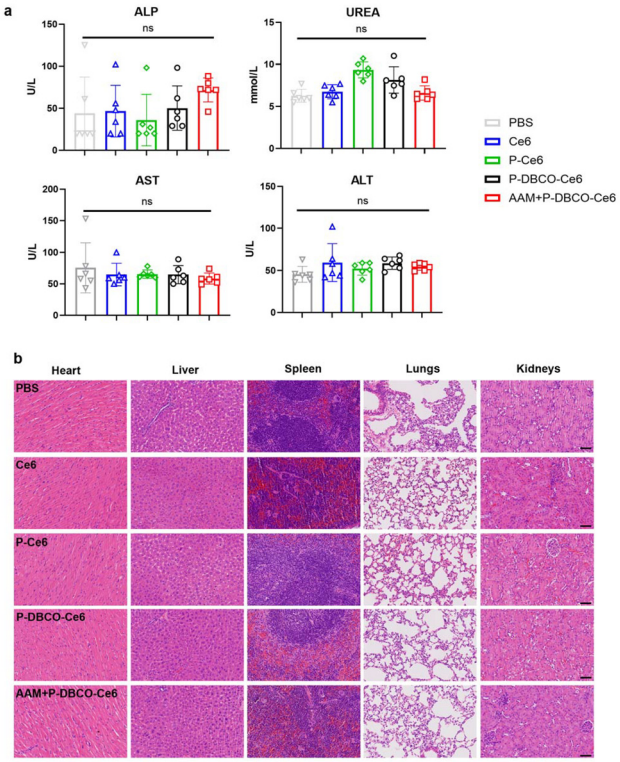

Fig. 6 PDT treatment biosafety analysis: (a) biochemical and blood routine evaluation of mice on day 16 after PDT treatment and (b) H&E staining of the major organs (heart, liver, spleen, lungs and kidneys) on day 16 after PDT treatment. Scale bar: 50 μm.

analysis revealed that major serum parameters, namely alkaline phosphatase (ALP), urea, aspartate aminotransferase (AST), and alanine aminotransferase (ALT), remained within normal ranges, comparable to the PBS control group (Fig. 6a). This suggests no significant impairment of liver or kidney function. Histological examination showed no discernible tissue damage (Fig. 6b). Collectively, these findings substantiate the biosafety of the bioorthogonal reaction-mediated PDT.

Conclusions

PDT based on photosensitizer–peptide conjugates has recently demonstrated remarkable antitumor potential in animal models. However, the limited cell membrane binding affinity and rapid systemic clearance have hindered their transition to clinical applications. By leveraging metabolic glycoengineering and bioorthogonal reactions, we have shown that a DBCO-decorated Ce6–peptide conjugate can covalently bind to the cell membrane and remain there for at least 24 h, significantly enhancing the PDT efficacy by inducing *in situ* cell membrane damage through lipid oxidation. Notably, a 3.3-fold increase in photosensitizer tumor accumulation was observed through an *in vivo* bioorthogonal reaction, which can lead to tumor ablation with a single PDT treatment. This research presents a novel strategy for improving the specificity and efficiency of

PDT, potentially paving the way for more effective cancer treatments.

Author contributions

Buwei Hu: conceptualization, methodology, formal analysis, investigation, data curation and writing – review and editing. Chenlin Ji: chemical synthesis support. Zhuohang Zhou: chemical synthesis support. Jianjun Cheng: project administration, resources, supervision, funding acquisition and writing – review and editing. Rui Sun: conceptualization, supervision, resources and writing – review and editing. The manuscript was written through contributions of all authors. All authors have given approval to the final version of the manuscript.

Data availability

Data will be made available upon request. The data supporting the finding of this study have been included as part of the ESI.†

Conflicts of interest

There are no conflicts to declare.

Acknowledgements

This work was supported by the National Natural Science Foundation of China (52233015), the New Cornerstone Investigator Program, the New Cornerstone Science Foundation, and the "Pioneer" and "Leading Goose" R&D Program of Zhejiang.

References

1 G. Gunaydin, M. E. Gedik and S. Ayan, *Front. Chem.*, 2021, **9**, 691697.
2 I. S. Mfouo-Tynga, L. D. Dias, N. M. Inada and C. Kurachi, *Photodiagn. Photodyn. Ther.*, 2021, **34**, 102091.
3 D. E. Dolmans, D. Fukumura and R. K. Jain, *Nat. Rev. Cancer*, 2003, **3**, 380–387.
4 U. Chilakamarthi and L. Giribabu, *Chem. Rec.*, 2017, **17**, 775–802.
5 A. Hak, M. S. Ali, S. A. Sankaranarayanan, V. R. Shinde and A. K. Rengan, *ACS Appl. Bio Mater.*, 2023, **6**, 349–364.
6 M. Lan, S. Zhao, W. Liu, C. S. Lee, W. Zhang and P. Wang, *Adv. Healthcare Mater.*, 2019, **8**, 1900132.
7 J. H. Correia, J. A. Rodrigues, S. Pimenta, T. Dong and Z. Yang, *Pharmaceutics*, 2021, **13**, 1332.
8 D. K. Newman, *Eye*, 2016, **30**, 202–210.
9 W. Wang, L. T. Moriyama and V. S. Bagnato, *Laser Phys. Lett.*, 2013, **10**, 023001.
10 F. Borgia, R. Giuffrida, E. Caradonna, M. Vaccaro, F. Guarneri and S. P. Cannavò, *Biomedicines*, 2018, **6**, 12.
11 J. Li, A. Wang, L. Zhao, Q. Dong, M. Wang, H. Xu, X. Yan and S. Bai, *ACS Appl. Mater. Interfaces*, 2018, **10**, 28420–28427.
12 M. Abbas, Q. Zou, S. Li and X. Yan, *Adv. Mater.*, 2017, **29**, 1605021.
13 Y. Fang, H. Ma, X. Zhang, P. Zhang, Y. Li, S. He, C. Sheng and G. Dong, *Eur. J. Med. Chem.*, 2024, **264**, 116047.
14 Y. Li, M. Zhang, H. Han, B. Zhang, J. B. Matson, D. Chen, W. Li and Y. Wang, *Chem. Eng. J.*, 2022, **436**, 135240.
15 K. Liu, R. Xing, Q. Zou, G. Ma, H. Möhwald and X. Yan, *Angew. Chem., Int. Ed.*, 2016, **55**, 3036–3039.
16 S. K. Dhillon, S. L. Porter, N. Rizk, Y. Sheng, T. McKaig, K. Burnett, B. White, H. Nesbitt, R. N. Matin, A. P. McHale, B. Callan and J. F. Callan, *J. Med. Chem.*, 2020, **63**, 1328–1336.
17 V. Apostolopoulos, J. Bojarska, T. T. Chai, S. Elnagdy, K. Kaczmarek, J. Matsoukas, R. New, K. Parang, O. P. Lopez, H. Parhiz, C. O. Perera, M. Pickholz, M. Remko, M. Saviano, M. Skwarczynski, Y. Tang, W. M. Wolf, T. Yoshiya, J. Zabrocki, P. Zielenkiewicz, M. AlKhazindar, V. Barriga, K. Kelaidonis, E. M. Sarasia and I. Toth, *Molecules*, 2021, **26**, 430.
18 Y. Gao, Q. C. Zheng, S. Xu, Y. Yuan, X. Cheng, S. Jiang, Kenry, Q. Yu, Z. Song, B. Liu and M. Li, *Theranostics*, 2019, **9**, 1264–1279.
19 G. Battogtokh, Y. S. Choi, D. S. Kang, S. J. Park, M. S. Shim, K. M. Huh, Y.-Y. Cho, J. Y. Lee, H. S. Lee and H. C. Kang, *Acta Pharm. Sin. B*, 2018, **8**, 862–880.
20 J. Zhao, S. Li, Y. Jin, J. Y. Wang, W. Li, W. Wu and Z. Hong, *Molecules*, 2019, **24**, 817.
21 Q. Li, S. Feng and G. Feng, *Sens. Actuators, B*, 2025, **422**, 136629.
22 W. Li, J. Yang, L. Luo, M. Jiang, B. Qin, H. Yin, C. Zhu, X. Yuan, J. Zhang, Z. Luo, Y. Du, Q. Li, Y. Lou, Y. Qiu and J. You, *Nat. Commun.*, 2019, **10**, 3349.
23 L. Jiang, S. Zhou, X. Zhang, C. Li, S. Ji, H. Mao and X. Jiang, *Nat. Commun.*, 2021, **12**, 2390.
24 S. Zhang, L. Yang, X. Ling, P. Shao, X. Wang, W. B. Edwards and M. Bai, *Acta Biomater.*, 2015, **28**, 160–170.
25 L. Pan, J. Liu and J. Shi, *Chem. Soc. Rev.*, 2018, **47**, 6930–6946.
26 P. L. Chen, P. Y. Huang, J. Y. Chen, Q. Y. Shi, Y. Y. Zhu, Y. Chen, L. H. Liu and X. Z. Zhang, *Biomaterials*, 2022, **286**, 121593.
27 M. Wu, X. Liu, H. Chen, Y. Duan, J. Liu, Y. Pan and B. Liu, *Angew. Chem., Int. Ed.*, 2021, **60**, 9093–9098.
28 X. Xu, S. Shabiti, X. Zhang, J. Zheng, N. Liang, Z. Wang, S. Yu, Y. Wang, S. Jiang, Z. Pan, W. Li and L. Cai, *Nano Today*, 2024, **56**, 102270.
29 M. Wang, J. Liu, M. Xia, L. Yin, L. Zhang, X. Liu and Y. Cheng, *Eur. J. Med. Chem.*, 2024, **265**, 116119.

30 V. Apostolopoulos, J. Bojarska, T. T. Chai, S. Elnagdy, K. Kaczmarek, J. Matsoukas, R. New, K. Parang, O. P. Lopez, H. Parhiz, C. O. Perera, M. Pickholz, M. Remko, M. Saviano, M. Skwarczynski, Y. Tang, W. M. Wolf, T. Yoshiya, J. Zabrocki, P. Zielenkiewicz, M. AlKhazindar, V. Barriga, K. Kelaidonis, E. M. Sarasia and I. Toth, *Molecules*, 2021, **26**, 430.
31 J. A. Prescher, D. H. Dube and C. R. Bertozzi, *Nature*, 2004, **430**, 873–877.
32 T. Cañeque, S. Müller and R. Rodriguez, *Nat. Rev. Chem.*, 2018, **2**, 202–215.
33 H. Y. Yoon, H. Koo, K. Kim and I. C. Kwon, *Biomaterials*, 2017, **132**, 28–36.
34 Y. Bo, J. Zhou, K. Cai, Y. Wang, Y. Feng, W. Li, Y. Jiang, S. H. Kuo, J. Roy, C. Anorma, S. H. Gardner, L. M. Luu, G. W. Lau, Y. Bao, J. Chan, H. Wang and J. Cheng, *Proc. Natl. Acad. Sci. U. S. A.*, 2023, **120**, e2302342120.
35 H. Wang, Y. Bo, Y. Liu, M. Xu, K. Cai, R. Wang and J. Cheng, *Biomaterials*, 2019, **218**, 119305.
36 H. Wang, R. Wang, K. Cai, H. He, Y. Liu, J. Yen, Z. Wang, M. Xu, Y. Sun, X. Zhou, Q. Yin, L. Tang, I. T. Dobrucki, L. W. Dobrucki, E. J. Chaney, S. A. Boppart, T. M. Fan, S. Lezmi, X. Chen, L. Yin and J. Cheng, *Nat. Chem. Biol.*, 2017, **13**, 415–424.
37 P. V. Chang, J. A. Prescher, E. M. Sletten, J. M. Baskin, I. A. Miller, N. J. Agard, A. Lo and C. R. Bertozzi, *Proc. Natl. Acad. Sci. U. S. A.*, 2010, **107**, 1821–1826.
38 L. K. Mahal, K. J. Yarema and C. R. Bertozzi, *Science*, 1997, **276**, 1125–1128.
39 P. Jastrząb, K. Narejko, H. Car and P. Wielgat, *Cancers*, 2023, **15**, 5103.
40 S. S. Pinho and C. A. Reis, *Nat. Rev. Cancer*, 2015, **15**, 540–555.
41 J. Daly, S. Sarkar, A. Natoni, J. C. Stark, N. M. Riley, C. R. Bertozzi, M. Carlsten and M. E. O'Dwyer, *Blood Adv.*, 2022, **6**, 3352–3366.
42 M. Jiang, Y. Liu, Y. Dong, K. Wang and Y. Yuan, *Biomaterials*, 2022, **284**, 121480.
43 L. Tang, Q. Yin, Y. Xu, Q. Zhou, K. Cai, J. Yen, L. W. Dobrucki and J. Cheng, *Chem. Sci.*, 2015, **6**, 2182–2186.
44 Y. Tu, Y. Dong, K. Wang, S. Shen, Y. Yuan and J. Wang, *Biomaterials*, 2020, **259**, 120298.
45 L. Mei, Y. Liu, J. Rao, X. Tang, M. Li, Z. Zhang and Q. He, *ACS Appl. Mater. Interfaces*, 2018, **10**, 17582–17593.
46 S. Wang, Y. Zhang, Y. Wang, Y. Yang, S. Zhao, T. Sheng, Y. Zhang, Z. Gu, J. Wang and J. Yu, *Nat. Commun.*, 2023, **14**, 6953.
47 J. Liu, F. Hu, M. Wu, L. Tian, F. Gong, X. Zhong, M. Chen, Z. Liu and B. Liu, *Adv. Mater.*, 2021, **33**, 2007888.
48 R. Xie, S. Hong, L. Feng, J. Rong and X. Chen, *J. Am. Chem. Soc.*, 2012, **134**, 9914–9917.
49 Y. Liu, S. Xu, Q. Lyu, Y. Huang and W. Wang, *Aggregate*, 2024, **5**, e443.
50 R. Zaman, R. A. Islam, N. Ibnat, I. Othman, A. Zaini, C. Y. Lee and E. H. Chowdhury, *J. Controlled Release*, 2019, **301**, 176–189.
51 T. Entradas, S. Waldron and M. Volk, *J. Photochem. Photobiol., B*, 2020, **204**, 111787.
52 T. Bakkum, T. van Leeuwen, A. J. C. Sarris, D. M. van Elsland, D. Poulcharidis, H. S. Overkleeft and S. I. van Kasteren, *ACS Chem. Biol.*, 2018, **13**, 1173–1179.
53 L. M. Fan and J. Li, *J. Pharmacol. Toxicol. Methods*, 2014, **70**, 40–47.
54 A. Gomes, E. Fernandes and J. L. F. C. Lima, *J. Biochem. Biophys. Methods*, 2005, **65**, 45–80.
55 K. Hirakawa, D. Ouyang, Y. Ibuki, S. Hirohara, S. Okazaki, E. Kono, N. Kanayama, J. Nakazaki and H. Segawa, *Chem. Res. Toxicol.*, 2018, **31**, 371–379.
56 M. Wang, M. Wu, X. Liu, S. Shao, J. Huang, B. Liu and T. Liang, *Adv. Sci.*, 2022, **9**, 2202914.
57 L.-H. Liu, W.-X. Qiu, Y.-H. Zhang, B. Li, C. Zhang, F. Gao, L. Zhang and X.-Z. Zhang, *Adv. Funct. Mater.*, 2017, **27**, 1700220.
58 D. Chen, Q. Xu, W. Wang, J. Shao, W. Huang and X. Dong, *Small*, 2021, **17**, e2006742.
59 M. Niedre, M. S. Patterson and B. C. Wilson, *Photochem. Photobiol.*, 2002, **75**, 382–391.
60 O. M. T. Pearce and H. Läubli, *Glycobiology*, 2015, **26**, 111–128.
61 T. Harayama and H. Riezman, *Nat. Rev. Mol. Cell Biol.*, 2018, **19**, 281–296.
62 D. Tsikas, *Anal. Biochem.*, 2017, **524**, 13–30.
63 H. Wang, M. C. Sobral, D. K. Y. Zhang, A. N. Cartwright, A. W. Li, M. O. Dellacherie, C. M. Tringides, S. T. Koshy, K. W. Wucherpfennig and D. J. Mooney, *Nat. Mater.*, 2020, **19**, 1244–1252.
64 H. Wang and D. J. Mooney, *Nat. Chem.*, 2020, **12**, 1102–1114.
65 Z. Gong, B. Zhou, X. Liu, J. Cao, Z. Hong, J. Wang, X. Sun, X. Yuan, H. Tan, H. Ji and J. Bai, *ACS Appl. Mater. Interfaces*, 2021, **13**, 55913–55927.

